machines

MDPI

Article

Numerical and Experimental Investigation of Pressure Pulsation in an LDPE Hyper-Compressor's Interstage Pipeline

Liya Ma [1], Xingyu Chen [2], Wei Xiong [2], Zenghui Ma [1] and Bin Zhao [2,*]

[1] Xinjiang Oilfield Gas Storage Co., Ltd., Hutubi 831200, China
[2] School of Power and Energy Engineering, Xi'an Jiaotong University, No.28 West Xianning Road, Xi'an 710049, China
* Correspondence: zhaobin0302@mail.xjtu.edu.cn

Abstract

A hyper compressor is one of the most critical pieces of equipment for synthesizing low-density polyethylene (LDPE) with a discharge pressure up to 350 MPa. Such a high discharge pressure creates significant challenges for safety and reliability. In this study, a 3D transient computational fluid dynamics (CFD) model of a hyper-compressor's interstage pipeline was adopted to examine the characteristics of pressure pulsation inside the interstage pipeline. First, flow channels of multiple poppets in the combined valve were simplified into a single channel while keeping the flow area identical. A single-degree-of-freedom equation was employed to calculate the dynamic motion of the simplified valve. Then, the acceleration, velocity, and lift of the valve were acquired by accumulating pressure-induced forces. Finally, the entire model was solved, and the p–θ diagram inside the working chambers and the pressure pulsation inside the interstage pipeline were acquired. It was found that the isotropic indexes of compression and expansion processes were 29.1 and 3.17 for the first stage of the hyper-compressor, and 36.85 and 3.65 for the second stage, respectively. The indices were significantly higher than those of the common compressor due to the higher compressibility of ethylene at hyper-pressures. The maximal pressure pulsations around the first stage and the second stage were 17.5% and 16.22%, respectively. Strain gauges were adopted to measure the on-site pressure pulsation. The results showed that the proposed CFD model was able to predict the coupling of thermodynamic processes in the working chamber and pressure pulsation in the pipeline. The comparison between the predicted and measured frequency vs. amplitude diagrams showed that the discrepancies at lower harmonics were smaller than those at higher harmonics. The maximum discrepancy of the dominant harmonic amplitudes between the CFD prediction and the strain gauge measurement was within approximately ±13%.

Keywords: CFD; LDPE; hyper-compressor; pressure pulsation

Check for updates

Academic Editor: Kim Tiow Ooi

Received: 27 August 2025
Revised: 15 July 2026
Accepted: 20 July 2026
Published: 24 July 2026

Copyright: © 2026 by the authors. Licensee MDPI, Basel, Switzerland. This article is an open access article distributed under the terms and conditions of the Creative Commons Attribution (CC BY) license.

1. Introduction

Low-density polyethylene (LDPE) has been widely used in many applications with the advantage of thermal and chemical resistance, resilience, and low cost [1]. During the process of synthesizing LDPE from ethylene, the ethylene had to be compressed by an ultra-high pressure of up to 350 MPa [2]. To meet this high demand, the hyper-compressor became one of the most critical pieces of equipment during the processes of multi-stage compression and was required to be highly reliable [3].

While working at such high pressure, the key components of the hyper-compressor, such as the valve and packing cup, suffer not only from ultra-high pressure but also from the fluctuation between the suction pressure and discharge pressure, which usually leads to the earlier failure of these components [4] that directly determine the availability and safety of the hyper-compressor. Based on the work of Mac Laren [5], Giacomelli et al. [6] took into consideration the effect of pressure pulsation in the suction and discharge chambers on valve motion and built the analytic model of valve dynamics using the equations referring to gas flow and the motion law of valves. In this analytic model, the flow coefficients affected by the valve profiles and stiction effect due to the use of lubrication oil are given by the experimental data. By solving this model, the valve lift, pressure in the working chamber, and pressure pulsation were acquired. The experimental and analytic results were in good agreement in terms of pressure drop and valve lift. The results were finally adopted as the basis of fault diagnosis of an LDPE compressor. Bianchini [7] identified that the pressure losses, drag forces, and flow coefficients varied during the opening and closing process using a 3D computational fluid dynamics model of the poppet valves. These dynamic pressure parameters were then considered in the 1D valve dynamic model to obtain a more accurate valve lift. Despite the highly accurate design of the valve lift, Bagagli [8] pointed out that the aforementioned model was inadequate to cover the most important failure of the valves. The author conducted an impact finite element analysis of the poppet valve to evaluate the stress under different impacting velocities and found that the maximum stress increased almost linearly with the increase in impact velocities. The damage and life of the poppet valve associated with each impact was then built according to the Palmgren–Miner rule. Finally, using the relationship between valve lift and impact velocity, the optimal valve geometry was acquired with a 15% and 60% reduction in pressure loss and backpressure, respectively. To improve the efficiency of the hyper-compressor, Maggi [9] performed a dedicated description of the valve design using the drag coefficient and flow coefficient as functions of the valve geometry. The results showed that an improvement in the drag coefficient resulted in a much larger flow rate and less power consumption. When ethylene has co-monomers, such as Vinyl Acetate, Methyl Acrylate, and Acrylic Acid, it tends to form wax and other types of fouling on the surface of the valve. The wax fouling on the valve could lead to leakage and higher discharge temperature, which may trigger the emergency shutdown of the compressor. Simpson [10] et al. compared the structure of the single poppet valve (SPV) and multi poppet valve and found that the SPV was less affected by the process of wax fouling because the single flow channel could not bypass another, thus allowing it to foul. However, the diameter and lift of the poppet in the SPV were much larger compared to those in the MPV, resulting in larger impact forces and higher discharge temperature. Besides the valve, the design of the packing cup is also important to ensure the safety and availability of the hyper-compressor. Maggi et al. [11] performed a thorough study of the autofrettage procedure of the packing cup to increase the safety factor during the manufacturing process, optimizing the compressive pre-stress on the lube oil hole. Taking into consideration of the external mechanical vibration, Stosiak et al. [12] presented an analytical and experiment investigation on the dynamic motion of the hydraulic valve and pointed out that the periodically variable throttling of the flowing liquid, which creates additional components in the pressure pulsation spectrum with frequencies equal to the frequencies of the vibrating valve body. Lei et al. [13] investigated the effect of the interference fit value on the stress distribution and evolution of the packing cup using the FEM and fatigue analysis. A much narrower but safer range of the interference fit value was acquired. Miller et al. [14] installed strain gauges on the outer surface of the packing cup to monitor pressure distribution and evolution during the working process of the hyper-compressor. The monitored pressures

were analyzed to evaluate the sealing performance. The author claimed that monitoring the pressure inside the packing cup was helpful for extending the life of the cylinder and optimizing cylinder change. Optimized design of critical parts is vitally important to the hyper-compressor. During the service process, adequate and reasonable transducers, such as temperature and pressure transducers, should be adopted to monitor the health of the compressor. Researchers have been dedicated to using various kinds of sensors to detect the early characteristics of failure modes. Park et al. [15] proposed a data-based multivariate statistical monitoring method to detect anomalies in the LDPE hyper-compressor with a weighted principal component analysis model (WPCA). The WPCA model can deal with time-dependent and time-independent components of data, combining principal component analysis (PCA). The results showed that five emergency shutdowns were identified successfully by the WPCA-based principal component control limit (PCCL). Above all, the importance of critical components design, condition monitoring, and fault diagnosis for the LDPE hyper-compressor has been widely accepted, and many studies have been performed with considerable progress.

However, during the working process, the intermittent opening and closing of the valves can produce pressure pulsation inside the valve chamber, and if not controlled, pressure pulsation can transfer downstream through the piping lines. This could lead to vibration, cyclic stress in the pipelines, and sometimes earlier failure of accessory equipment. Under ultra-high pressure, the thermodynamic properties became close to those of a liquid with dense density and very high sound speed. The effect of the normally used buffer tank and silencer on attenuating pressure pulsation was either limited or extraordinarily expensive. Many researchers have focused on the method of controlling pressure pulsation reasonably. Giacomelli et al. [16] deduced the basic equations for pressure pulsation, assuming the pressure pulsation was formed by small perturbations. Based on basic equations, a numerical program was developed and calibrated by various on-site compressors. The author suggested that a preliminary acoustic study should be performed, and the consequent shaking force should be adopted to check the suitability of all the supports. Karpenko [17] provided an analysis of the hydrodynamic processes and flow characteristics of an aircraft pipeline system by using the NS equations and the k-epsilon turbulence model. The research confirmed that utilizing the equivalent length method and equivalent length same shape method is inappropriate for investigating angular fitting connections. Bai et al. [18] simulated the discharge pipeline of an LDPE compressor to acquire the natural frequencies (NFs) and to exclude the possibility of gas column resonance. Then, a vibration model was built to check the NFs of the solid pipeline, and wooden supports were added properly to acquire a satisfying vibration level. Carcasci and Sacco [19] reported a case that occurred in a polyethylene plant, where excessive vibration led to rupture and flammable gas leakages. After careful examination, the author identified that the reason for this accident was that the compressor was revamped, but the pipeline, supports, and other accessory equipment could not adapt to the change in the compressor. After re-calculation of the pulsation and vibration of the mechanical pipeline system, newly designed supports were added to reduce excessive vibrations. For an LDPE plant, the vibration of the pipeline can be detected by an accelerometer, but the normally intrusive pressure sensors were not allowed to be used. To measure the pressure pulsation of the LDPE pipeline, Carcasci et al. [20] employed a strain gauge to build an indirect measurement method. By sticking two orthogonal strain gauges along the circumferential and axial directions of the pipeline, the circumferential and axial strains can be measured. According to Hooke's law for linearly elastic isotropic material, the relationship between internal pressure and the two strains can be acquired. The author performed more than 450 measurements to validate this method, and it was proven to be highly reliable. Fusi et al. [21], Geng et al. [22], and Xiao and Geng [23] also

adopted this strain gauge method to measure the on-site pressure pulsation of the LDPE pipeline, alongside various methods to reduce excessive vibration, and the results were all satisfying. Yang et al. [24] built a 3D computational fluid dynamics model of an LDPE compressor and its pipelines to examine the thermodynamic performance of the compressor and characteristics of pressure pulsation inside the pipeline. The author promoted the strain gauge method from detecting pressure pulsation to measuring the dynamic pressure inside the compression chamber of the compressor by sticking the strain gauge onto the surface of the plunger. The comparison between the numerical and measured pressure agreed well with each other. Stosiak et al. [25] analyzed the dynamic pressure waveforms in hydraulic hoses using a four-piece hydraulic model. The verified hydraulic model laid a solid foundation for designing a precise and reliable hydraulic system.

At present, the pressure pulsation of LDPE compressors is commonly predicted using either plane–wave theory or one-dimensional unsteady-flow methods. However, plane–wave theory is based on small-perturbation assumptions and therefore involves considerable simplification, while one-dimensional unsteady-flow methods are limited in their ability to represent complex flow geometries and multiphase working media. In particular, when the working medium contains EVA, an effective model is still lacking for accurately predicting the pressure pulsation characteristics of LDPE hyper-compressors. To address this issue, the present study develops a coupled transient CFD framework for the interstage pipeline of an LDPE hyper-compressor. In this framework, the dynamic motion of the poppet valve is described using a one-degree-of-freedom motion equation. The coupling between valve motion and pressure pulsation is achieved by calculating the transient fluid forces acting on the valve, from which the valve acceleration, velocity, and displacement, namely valve lift, are subsequently obtained.

2. Numerical Model

2.1. Simplified Model for the MPV

The investigated hyper-compressor has two stages, which compress ethylene from 28 MPa to 109 MPa in the first stage and 108 MPa to 260 MPa in the second stage. The valve for the hyper-compressor has a combined structure in which the suction poppet and discharge poppet share a common valve seat, as shown in Figure 1. The other components in the combined valve include the suction poppet, the limiter of the suction poppet, the springs, the discharge poppet, the limiter of the discharge poppet, and the disk springs. The combined valve for the first stage has a total of 12 poppets, of which 6 work as suction poppets and the other 6 are the discharge poppets. The secondary valve has a similar structure to the first stage but uses a total of 8 poppets, of which half are suction poppets and the other half are discharge poppets.

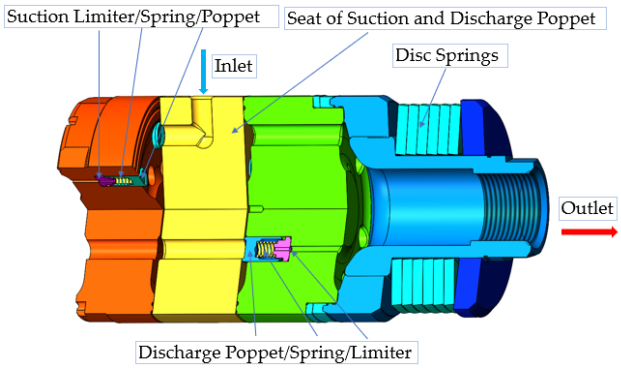


Figure 1. Solid model of the multi-poppet valve.

The combined valve for the first/second stage of the compressor has 6/4 inlet holes in the radial direction and 1 outlet in the axial direction. The detailed geometry dimensions of the suction and discharge poppet are listed in Table 1. To prevent leakage through the poppet, a pre-compression length of 2/2.2 mm was designed for the valves of the first and second stage.

Table 1. Detailed geometry dimensions of the suction and discharge poppets.

	Item	Diameter [mm]	Stiffness of Spring [N/mm]	Lift [mm]	Mass [g]	Pre-Compression [mm]
First Stage	Suction Poppet	22.9	11,400	2.6	60	2
	discharge Poppet	22.9	11,400	2.2	60	2
Second Stage	Suction Poppet	23	14,200	2.4	64	2.2
	Discharge Poppet	23	14,200	2.0	64	2.2

To acquire the flow domain inside the combined valve, the Design Modeler of ANSYS 2024 was adopted using the Boolean operation. The acquired flow domain for the first stage is shown in Figure 2. A partial clearance chamber inside the compression chamber was added in the flow domain, as shown on the left in Figure 2.

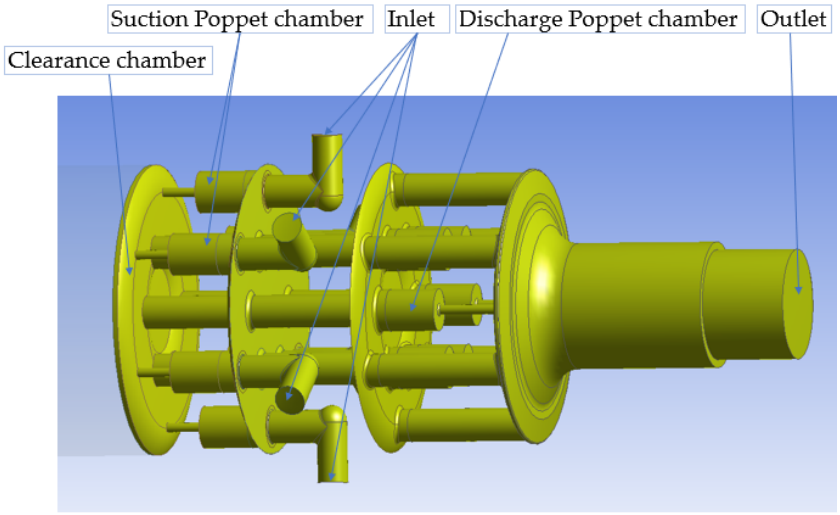


Figure 2. Flow domain of the combined valve in the first stage.

As shown in Figure 2, the geometric feature of the flow domain inside the combined valve is complex. To reduce the computational cost, the six flow channels associated with the six suction/discharge poppets are merged into a single channel. Then, the flow domain inside the combined valves is reconstructed, as shown in Figure 3. The simplified model may smooth local flow non-uniformity and localized loss near individual poppets, which may partly lead to the differences at higher harmonics.

In order to verify the feasibility of the simplified model, a static flow simulation test was conducted, and the results showed that the relative deviation of the flow pressure difference and mass flow rate between the simplified model and the original model was less than 1%, as shown in Table 2.

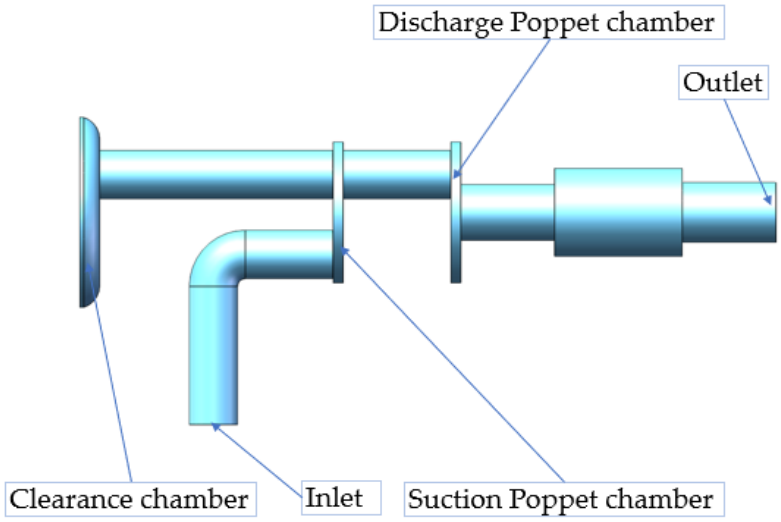


Figure 3. Simplified flow domain of the combined valve in the first stage.

Table 2. Pressure drop and mass flow rate deviation.

Model	Pressure Drop [MPa]	Mass Flow Rate [kg/s]	Deviation of Pressure Drop [%]	Deviation of Mass Flow Rate [%]
Original Valve	0.395	2.426	-	-
Equivalent single channel valve	0.392	2.434	0.76	0.33

Then, the flow domain of the combined valve is separated into several sub-domains to generate a high-quality mesh, of which the detail has been described in our previous work [26]. The sub-domains of the flow channel inside the combined valve are then merged by setting interfaces between the coincident surfaces. The final discrete model for the clearance chamber and working chamber with an element/node of 243,047/129,189 is shown in Figure 4. The location of the upper surface of the suction/discharge poppet, the inlet and outlet of the combined valve, and the wall of the plunger are shown in Figure 4. The discrete model of the secondary combined valve can be acquired following the same procedure.

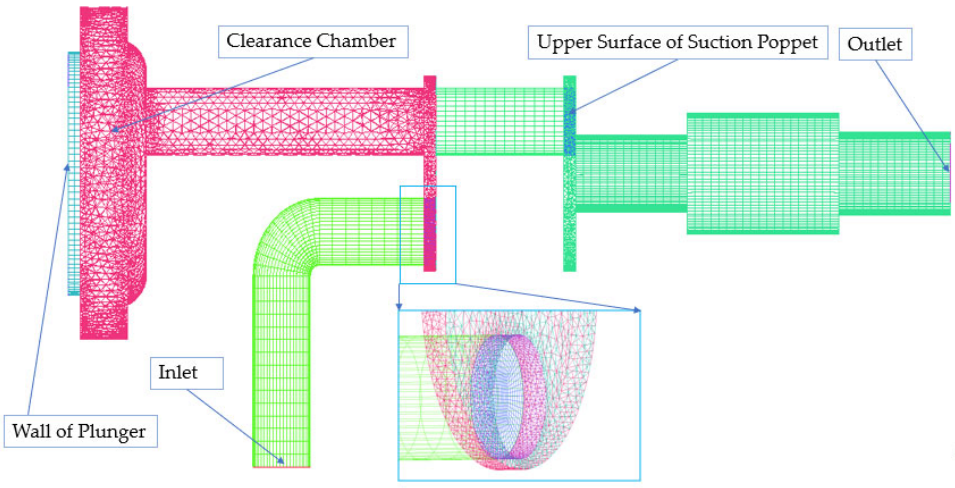


Figure 4. Discrete model for the combined valve and clearance chamber.

After the discrete model of the first and second combined valve is obtained, the valve dynamics can be calculated according to a single-degree-of-freedom equation to realize the interaction between poppet motion and pressure pulsation inside the pipelines. This equation is expressed as follows:

$$Ma + Cv + Kl = \sum_{i=1}^{i=N} \int pdA + F_s \quad (1)$$

where a, v, and l are the acceleration, speed, and lift of the poppet; M, C, and K are the equivalent mass of the poppet and spring, and the damping ratio and stiffness of the spring. $\int pdA$ represent the pressure-induced forces acting on the surfaces of the poppet; N is the number of suction/discharge poppets in a single combined valve; and F_s represents the spring forces generated from pre-compression.

As shown on the left in Figure 4, the plunger is located at the top dead center (TDC), which means the plunger is pushed to the farthest location away from the crankshaft. The plunger is driven by a crankshaft-connecting rod mechanism, which transfers the rotational movement of the crankshaft into the reciprocating movement of the plunger. The reciprocating speed of the plunger can be described by the rotational speed of the crankshaft, n; the radius of the crankshaft, R; the length of the connecting rod, L; and the angle between the crankshaft and connecting rod, θ.

$$v = \frac{4Rn\pi}{60}\left(\sin\theta + \frac{R/L}{2}\frac{\sin 2\theta}{\sqrt{1-(R/L)^2\sin^2\theta}}\right) \quad (2)$$

The key dimensions of the first and secondary stage cylinders are listed in Table 3, where the first subscript represents the first stage and the second subscript represents the second stage; D_{1st} and D_{2nd} are the diameters of the first and second plunge stages.

Table 3. Dimensions of the cylinder and valve.

Item	Value	Item	Value
D_{1st} (mm)	88	R_{1st} (mm)	190
D_{2nd} (mm)	80	R_{2nd} (mm)	170
L_{1st} (mm)	800	L_{2nd} (mm)	800
n (rpm)	200		

2.2. Meshes for Interstage Pipeline

As shown in Figure 5, two cylinders operate during the first and second stages of the hyper-compressor. The interstage pipeline starts from the outlet of the combined valves of the first-stage cylinders A and B, and combines at the discharge buffer tank, as shown in Figure 5. After flowing through the discharge buffer tank, the flow is separated into two tributaries and then each tributary is separated into two sub-tributaries before entering the interstage cooler. After cooling, the four sub-tributaries merge into one main flow. The cooled main flow enters the suction buffer tank of the second stage, and then separates into two tributaries before entering the combined valve of the second-stage cylinders A and B.

By using the ICEM of ANSYS 2024 the discrete flow domain of the interstage pipeline can be acquired, as shown in Figure 6.

Then, the discrete model of the combined valves, as shown in Figure 4, and the discrete model of the interstage pipeline, as shown in Figure 6, were assembled to obtain the entire CFD model of the interstage flow of the hyper-compressor. During the simulation, multiple mesh sizes are generated for the flow domain of the compressor cylinders and the pipelines,

respectively, taking into consideration their different geometric features. Mesh sizes of 2, 3, 4, and 5 mm were selected to generate the mesh for the working chamber; sizes of 0.4, 0.8, 1.2, and 1.6 mm in the radial direction and 20, 40, 60, and 80 mm in the axial direction were used to generate the mesh for the pipeline. Local refinement took place in the transition region, such as the inlet/outlet of the buffer tank, and the junction of the pipe. To ensure the CFD model converged, the pressure pulsation of the monitored points in two consecutive cycles did not exceed 1% at any angle of the cycle. Then, the pressure pulsation at the outlet of cylinder A and the CPU time were used to select the proper mesh size, as shown in Table 4.

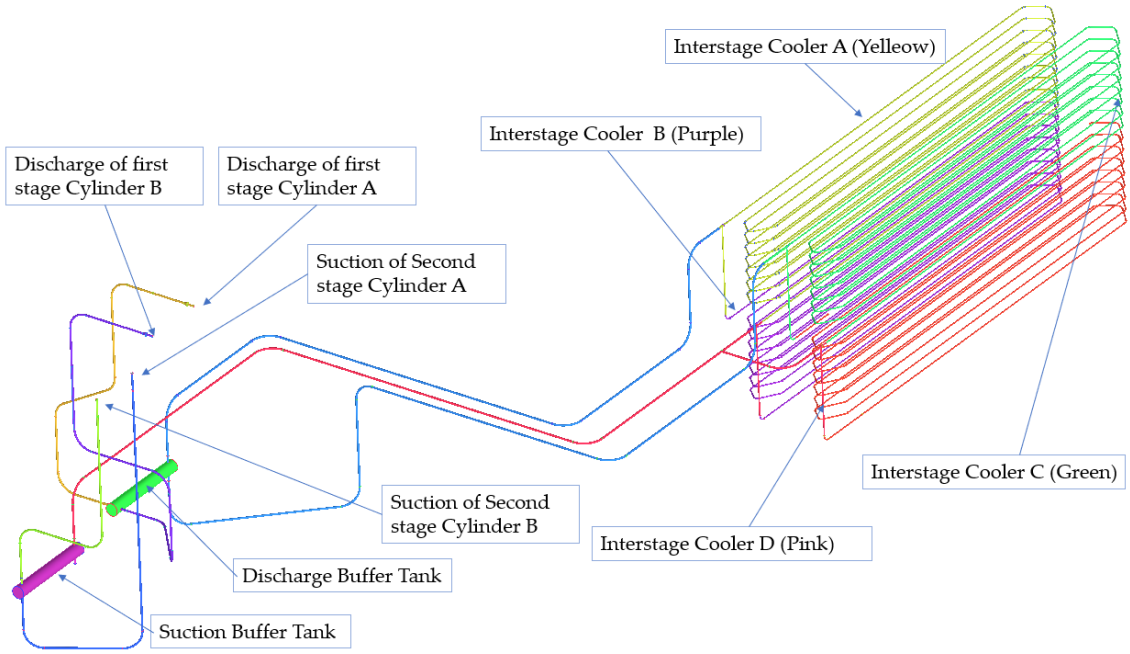


Figure 5. Physical model of the interstage pipeline.

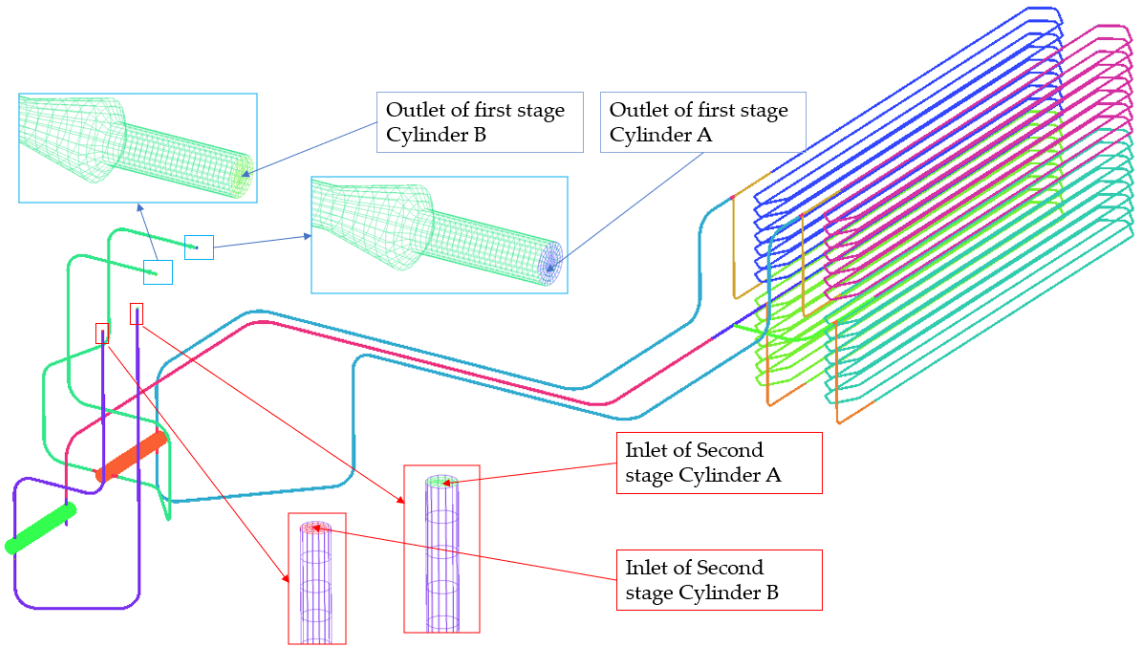


Figure 6. Discrete model of the interstage pipeline.

Table 4. Mesh Independence check.

Case	Cylinder Mesh [mm]	Pipeline Radial [mm]	Pipeline Axial [mm]	Elements [$\times 10^6$]	Pressure Pulsation [%]	Average CPU Time per Cycle [h]
Case 1	5	1.6	80	1.792	14.52	~8.3
Case 2	4	1.2	60	2.315	15.71	~10.5
Case 3	3	0.8	60	2.808	16.20	~12.1
Case 4	2	0.4	40	4.216	16.34	~17.7

Finally, the mesh sizes of Case 3 in Table 4 were used for the compressor cylinders and pipelines as a compromise between accuracy and computational cost. The entire model had a total of 2,807,630/2,002,150 elements/nodes with a computational cost of ~12 h per cycle, as shown in Figure 7.

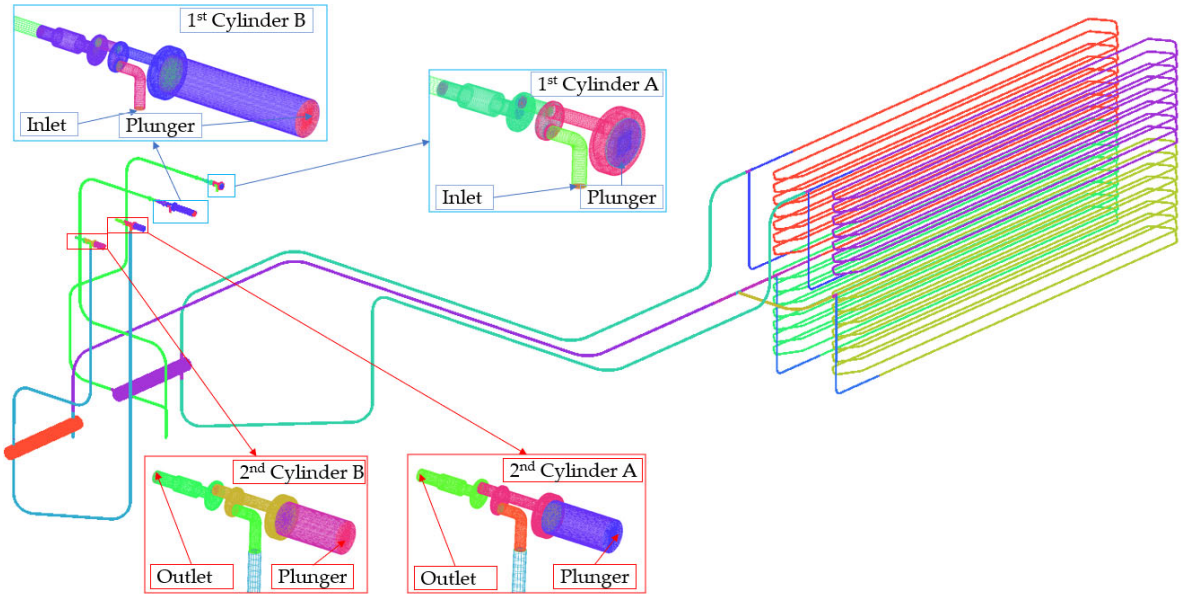


Figure 7. The entire CFD model of the interstage pipeline.

As shown in Figure 7, two cylinders operate during the first stage, 1st cylinder A and 1st cylinder B, and two cylinders operate during the second stage, 2nd cylinder A and 2nd cylinder B. Two inlets and two outlets of the entire model are located in the four above-mentioned cylinders, respectively. The phase angle of the 1st cylinder A was set as 0°, and the relative phase angles of 1st cylinder B, 2nd cylinder A, and 2nd cylinder B corresponding to 1st cylinder A were 180°, 270°, and 90°. As a result, the plunger of the 1st cylinder A is in the TDC location, and the plunger of the 1st cylinder B is in the BDC location. The plunger of the 2nd cylinder A moves toward TDC, and the 2nd cylinder B's plunger moves toward BDC. Moreover, based on the relative phase angle, these four cylinders can experience the end of the discharge, suction, compression, and expansion processes.

2.3. Governing Equations and Thermodynamic Properties of Ethylene

The mass, momentum, and energy equations were employed as the governing equations to describe the working process of the hyper-compressor and flow inside the interstage

pipeline. Unsteady compressible RANS equations were selected to solve the numerical model, as follows:

$$\frac{\partial \rho}{\partial t} + \frac{\partial}{\partial x_j}(\rho \cdot u_j) = 0 \tag{3}$$

$$\frac{\partial}{\partial t}(\rho \cdot u_i) + \frac{\partial}{\partial x_j}(\rho \cdot u_i \cdot u_j) = -\frac{\partial p}{\partial x_j} + \frac{\partial \tau_{ij}}{\partial x_j} \tag{4}$$

$$\frac{\partial}{\partial t}(\rho \cdot h) + \frac{\partial}{\partial x_j}(\rho \cdot u_j \cdot h) = \frac{\partial p}{\partial t} + u_j \frac{\partial p}{\partial x_i} + \tau_{ij} \frac{\partial u_i}{\partial x_j} \frac{\partial u_j}{\partial x_i} \tag{5}$$

where τ_{ij} is the stress tensor, which is expressed as follows:

$$\tau_{ij} = \mu\left(\frac{\partial u_i}{\partial x_j} + \frac{\partial u_j}{\partial x_i} - \frac{2}{3}\delta_{ij}\frac{\partial u_k}{\partial x_k}\right) \tag{6}$$

To predict pressure pulsation, the accuracy of the thermodynamic properties of the working medium ethylene is of vital importance; this can be assessed using professional NIST software in which thermodynamic properties are calculated based on Helmholtz equation of state [27]. The major effects of placing ethylene under hyper-pressure are its incompressibility and water-like consistency at ambient temperatures and pressures. The indices of the compression/expansion processes are significantly higher than the common working condition, which has a direct effect on the pressure pulsation level in the pipeline system of the hyper-compressor. Since the suction pressure/temperature applied during the first stage is around 28 MPa/313 K and the discharge pressure/temperature is around 260 MPa/363 K, thermodynamic properties, such as density, heat capacity, sound speed, etc., were assessed in a range of temperatures [250, 400 K] and pressures [20.0, 300.0 MPa]. A table of thermodynamic properties for a range of temperatures and pressures was formed in the solver of Fluent. The temperature and pressure intervals of 0.5 K and 0.5 MPa were adopted to linearly interpolate the thermodynamic properties of ethylene.

2.4. Boundary and Initial Conditions

For the pressure pulsation model of the hyper-compressor's interstage pipeline, as shown in Figure 7, the average pressure and temperature of 28 MPa and 313 K were set as the boundary conditions for the inlets located in 1st cylinder A and 1st cylinder B. At the same time, the average pressure and temperature of 260 MPa and 313 K were set as the boundary conditions for the outlets located in the 2nd cylinder A and 2nd cylinder B. The average pressure of 109 MPa was set as the initial pressure of the interstage pipeline. According to the field data, the discharge temperature of the first stage was about 363 K, and the discharge pressure was 109 MPa. Taking the cooling effect of the interstage cooler into consideration, a steady CFD model was first solved to determine the temperature distribution in the interstage cooler. In the steady CFD, the temperature of the pipelines before cooling was set as 363 K, and the temperature of the cooler and pipelines afterward was set as 313 K. A heat transfer coefficient of 24 W/(m^2·K) was set as the wall condition of the interstage cooler. The boundary condition for the inlet was switched to a pressure inlet with a pressure/temperature of 109 MPa/363 K, and the boundary condition for the outlet was switched to a pressure outlet with a pressure/temperature of 108 MPa/313 K. After approximately 12,700 timesteps, the monitored temperatures at the elbows along the interstage cooler were compared to the field temperatures, and the maximal discrepancy was less than 3 K, which was taken as the criterion of convergence. The acquired steady temperature distribution is shown in Figure 8.

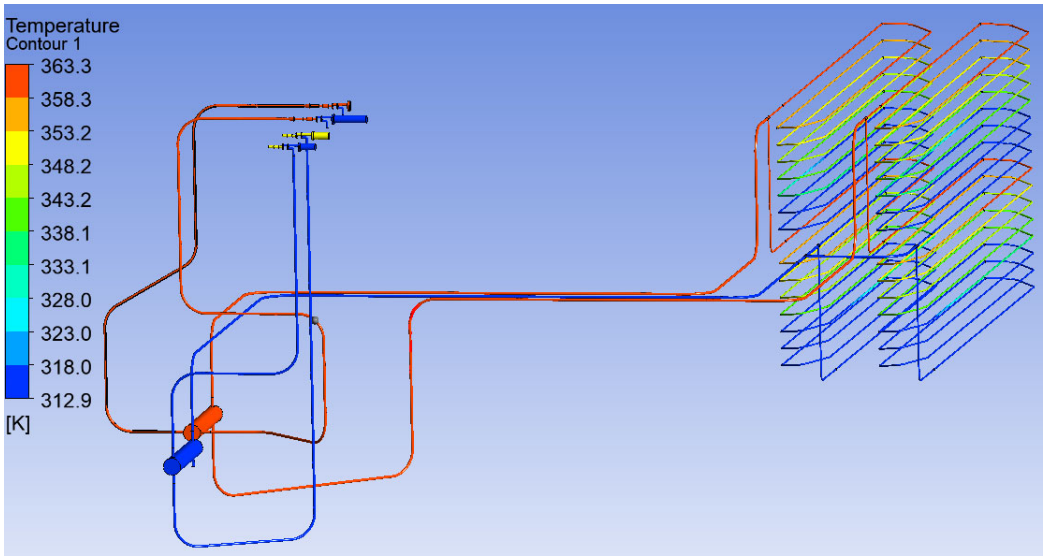


Figure 8. Steady temperature distribution of the interstage pipeline.

For this two-stage hyper-compressor, the inlet was located at the suction port of the first stage, and the outlet was located at the discharge port of the second stage. Therefore, the boundary conditions for the pressure of the inlets were set at 28 MPa/313 K, and the pressure of the outlets was set at 260 MPa/353 K, respectively. The discharge pressure/temperature of the first stage was determined to be 108 MPa/363 K. These conditions were further employed to mitigate the improper pressure and temperature distribution in the domains acquired during the steady simulation.

The patched temperature and pressure distributions were taken as the initial condition to solve the transient pressure pulsation inside the interstage pipeline. The combination of the RNG k–ε turbulence model, Pressure Implicit, with the Splitting of Operators (PISO) algorithm, the second-order upwind scheme, and the second-order backward Euler scheme was chosen to solve the thermodynamic processes in the reciprocating compressor and the pressure pulsation in the pipelines. The RNG k–ε model was selected because the present work focuses on pipeline-scale pressure pulsation and dominant harmonic components rather than resolving local turbulent eddies near each poppet. A previous comparison between RNG k–ε and DES showed that DES slightly improved the prediction of pressure pulsation but increased the computational cost by approximately four times. Considering the full-scale geometry, dynamic valve motion, and the need to simulate several compressor cycles, RNG k–ε was adopted as a practical compromise between accuracy and computational cost [24,26,28].

The time step was limited by the movement speed and the height of the mesh across the valve plate. A time step of 0.0004 s corresponding to a crank angle step of 0.48° was finally decided after a few attempts because a larger time step could lead to a negative mesh and failure of the calculation process due to the dynamic motion of the valve plate. The pressures inside the cylinders during the first stage, second stage, and the pressure inside the interstage pipelines were all taken as criteria to verify convergence. Convergence was defined as the deviation of pressure between two successive cycles smaller than 1%. The 3D CFD model of the interstage pipeline was solved using two CPUs, each with 56 available cores. It took about 12 h to complete a cycle of the physical model, and after about five cycles, the converged pressure inside the first and second stages of the four cylinders was acquired, as shown in Figure 9.

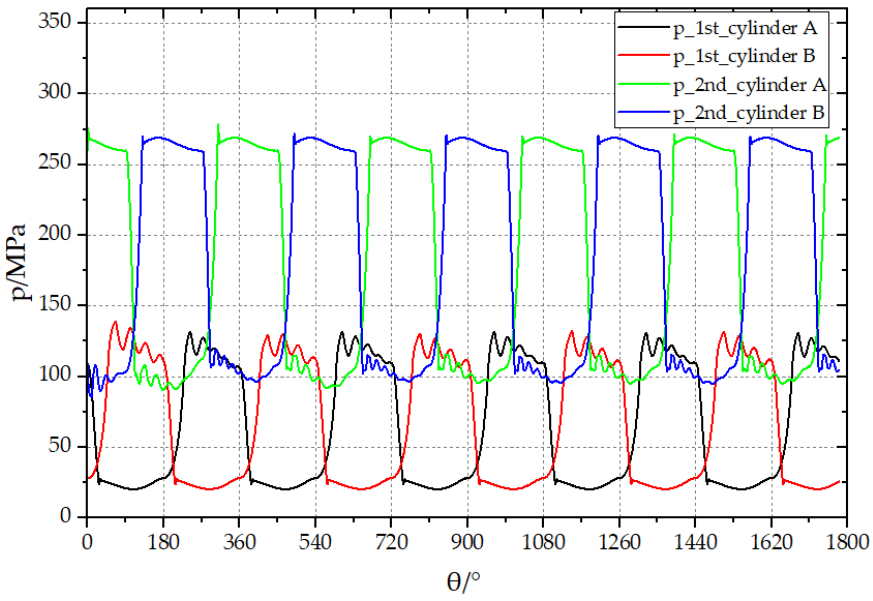


Figure 9. Pressure inside the first and second stages of the cylinders.

3. Field Test of the Pressure Pulsation

3.1. Measuring Principle

Due to the ultra-high pressure and the potential hazards of explosive ethylene, normal pressure sensors and transducers were intrusive to the measurements and, thus, were prohibited from use since they require direct contact with ethylene. Therefore, non-intrusive strain gauges were adopted to measure the internal pressure pulsation of the interstage pipeline, as used by Carcasci et al. [20].

The fundamental theory of measuring the strain of the outer surface induced by the internal pressure is explained. As shown in Figure 10, a pipe with an outer diameter of $2R_o$, and an internal diameter of $2R_i$, withstanding the internal p_i, circumferential σ_c, and axial stress σ_l is expressed as follows:

$$\sigma_c = 2 \cdot \sigma_a = p \cdot \frac{2 \cdot R_i^2}{R_o^2 - R_i^2} \tag{7}$$

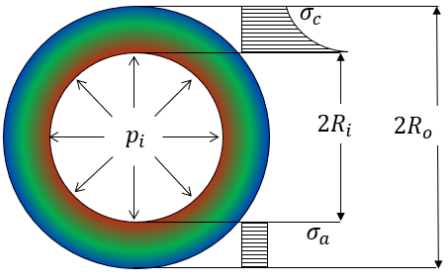


Figure 10. The circumferential and axial stress induced by internal pressure.

According to Hook's law for linearly elastic isotropic material, the relation between strain and stress can be written as follows:

$$\varepsilon_c = \frac{\sigma_a - \nu \cdot \sigma_c}{E} \tag{8}$$

$$\varepsilon_a = \frac{\sigma_c - \nu \cdot \sigma_a}{E} \tag{9}$$

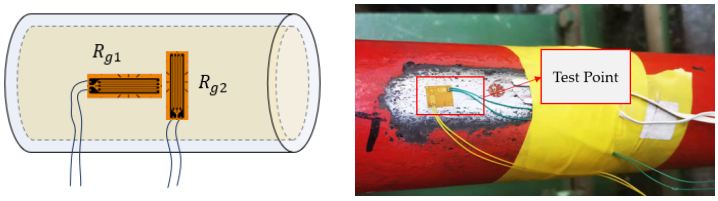
Then, the internal pressure is represented by the measured strain as follows:

$$p = \frac{\mathrm{E}}{1-\nu^2} \cdot \frac{R_o^2 - R_i^2}{2 \cdot R_i^2} \cdot (\varepsilon_c + \nu \cdot \varepsilon_a) \tag{10}$$

where E and ν represent the elastic modulus and Poisson's ratio of the measured pipe.

3.2. Measurement Method

Usually, two strain gauges are attached to the outer surface of the pipe in the circumferential and axial directions to measure the strain in each direction, as shown in Figure 11. Figure 11a,b presents a schematic diagram of the field test arrangement of strain gauges, respectively. The adopted strain gauges were made of Cu-Ni alloy with a model of Kyowa KFGS-5-120-C1-11, a dimension of 5 × 1.4 mm, and a typical electrical resistance of 120 Ω ± 0.4%. To install the strain gauge, the coating on the surface of the pipe was wiped out with sandpaper. Then, the strain gauges were attached to the pipe with glue. Together with the 1/4 Wheatstone bridge circuit and data acquisition system formed by NI 9237 and cDAQ-9174, the strains could be obtained and transferred into internal pressures inside the pipeline.



(**a**) Schematic diagram. (**b**) Field test.

Figure 11. Arrangement of the strain gauges.

The location of the testing point should be kept away from the nozzle, flange, and pipe supports, where the stiffness of the testing points is significantly higher than the nominal pipe, causing the measured data to not reflect the relationship between strain and internal pressure. The LDPE plant has many pieces of rotary equipment driven by electric motors, which generate magnificent electromagnetic interference, leading to the compromise of the test signal. Therefore, we replaced the DC source with a dry battery, and the entire test rig was covered by an electromagnetic interference shielding cover. Then the measurement was re-conducted, and the results showed much better agreement with each other.

A total of 14 test points were arranged along the discharge port of the first-stage cylinders to the discharge buffer tank, the four interstage coolers, the suction buffer tank, and the suction port of the second-stage cylinders, as shown in Figure 12. The pressure pulsation of the specific test points was also monitored in the CFD model.

3.3. Signal Processing and Uncertainty Analysis

Before the field measurement, the strain–pressure relationship was calibrated in the laboratory using a pipe with the same material and dimensions as the on-site pipe. The calibration was repeated five times over the pressure range of 10–300 MPa with an interval of 10 MPa. Three reference pressure transducer with full-scale ranges of 100, 200, and 300 MPa and an accuracy of 0.5% were used to cover the whole calibration range. For dynamic pressure measurement, additional uncertainty sources were considered, including bridge circuit noise, data acquisition resolution, electromagnetic interference, temperature drift, strain gauge installation, signal filtering, FFT leakage, and possible structural vibration

coupling. For the dynamic pressure pulsation measurement, a simplified uncertainty analysis was adopted. The calibration relationship was expressed as

$$p = a + bx \tag{11}$$

where p is the internal pressure, x is the measured strain, and b is the strain–pressure calibration coefficient.

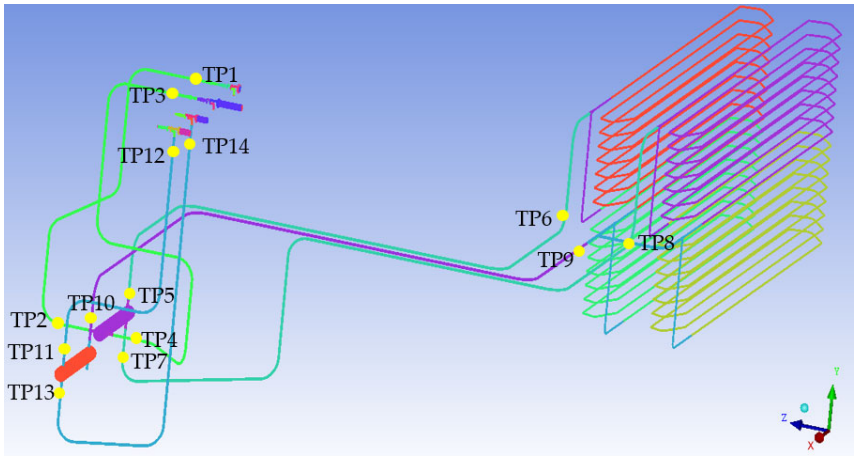


Figure 12. Arrangement of the strain gauges.

Since only the dynamic component of the pressure signal was analyzed, the mean value was removed from each record, and the pressure pulsation was calculated as

$$p'(t) = bx'(t) \tag{12}$$

where $x'(t) = x(t) - \overline{x}$. The strain records were divided into integer compressor cycles according to the rotational speed. The harmonic amplitudes were calculated using DFT. No additional smoothing filter was applied to the main harmonic components, so that the amplitudes of the pressure pulsations would not be artificially attenuated.

The uncertainty of the dynamic pressure amplitude was mainly attributed to the uncertainty of the calibration coefficient and the repeatability of the dynamic strain amplitude. The calibration coefficient b was obtained by linear regression of the calibration data, and its standard uncertainty u_b was taken as the standard error of the regression slope. For the dynamic signal, the uncertainty of the strain amplitude $u(A_x)$ was evaluated from the cycle-to-cycle repeatability. The dynamic pressure amplitude was calculated as $A_p = bA_x$, and its combined standard uncertainty was calculated as

$$u(A_p) = \sqrt{(A_x u_b)^2 + (buA_x)^2} \tag{13}$$

For peak-to-peak pressure pulsation, $\Delta p = b\Delta x$, and the corresponding uncertainty was calculated as

$$u(\Delta p) = \sqrt{(\Delta x u_b)^2 + (bu\Delta x)^2} \tag{14}$$

When the pressure pulsation was expressed as a percentage, $\eta = \Delta p/\overline{p} \times 100\%$, the uncertainty of the mean pressure was further included. The expanded uncertainty was obtained using a coverage factor of 2.

4. Results and Discussion

4.1. p–V Diagrams of the Two-Stage Hyper-Compressor

The p–θ diagram representing the cyclic working processes inside the four cylinders is depicted in Figure 13. As can be seen, the suction/discharge pressure of the first stage reached around 28/109 MPa, and the suction/discharge pressure of the second stage reached around 108 MPa/260 MPa. As the phase angle of the first cylinder A was set at 0°, the relative phase angles of the first cylinder B, the second cylinder A, and the second cylinder B were 180°, 270°, and 90°, respectively. The working processes inside the last three cylinders were relatively slower than those in the first cylinder A. The working processes inside the cylinder can be divided into four phases, i.e., expansion, suction, compression, and discharge. The durations of these four phases in the first cylinder A were [0°, 26.3°], [26.3°, 180°], [180°, 230.07°], and [230.07°, 360°]. Because of the pressure pulsation inside the interstage pipeline, the discharge processes of the first-stage cylinders and the suction processes of the second-stage cylinders fluctuated much more significantly than the discharge processes of the second-stage cylinders and the suction processes of the first-stage cylinders, respectively. Figure 13 shows the crank-angle-resolved pressure histories in the four cylinders. Because the two first-stage cylinders and the two second-stage cylinders operate with different phase angles, the discharge flow from the first stage and the suction demand of the second stage are not continuous but periodically superposed in the interstage pipeline. Therefore, the cylinder pressure is not only determined by the plunger motion and valve dynamics but also affected by the transient pressure feedback from the interstage pipeline. This explains why the discharge processes of the first-stage cylinders and the suction processes of the second-stage cylinders exhibit stronger fluctuations than the first-stage suction and second-stage discharge processes.

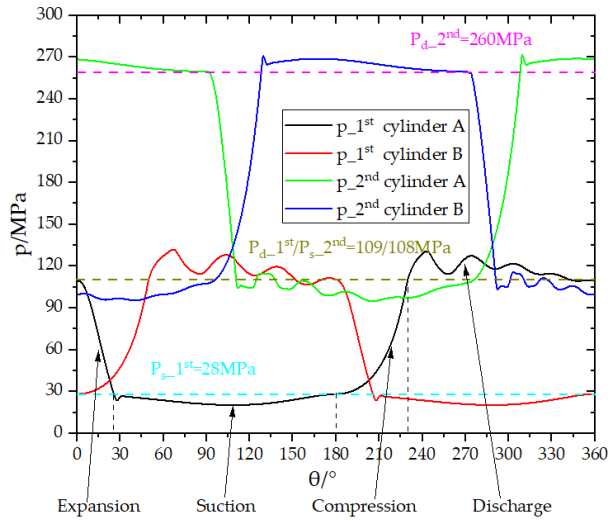


Figure 13. p–θ diagrams inside the four cylinders.

As shown in Figure 14, the p–V diagram was calculated based on the p–θ diagram, where V is the volume of the working chamber. The relative clearances in the first and second stages were about 14.78% and 17.88%. According to the curves of the compression and expansion process, the polytropic indices of these processes were calculated based on the volumes and pressures at the start and end of the compression and expansion curves. The polytropic indexes of compression and expansion in the first-stage cylinders were 29.1 and 3.17, and the polytropic indexes of compression and expansion in the second-stage cylinders were 36.85 and 3.65. Both the polytropic indices of the compression and expansion

processes were larger than those of a common air compressor at around 1.4, and these indices were compared to the isentropic indices. Meantime, the polytropic compression and expansion indices in the second-stage cylinders were larger than those of the first-stage cylinders. As aforementioned, the rotational speed of the hyper-compressor was 200 rpm, from which the power consumption during the cyclic process accumulated. The area enclosed by each p–V loop represents the indicated work of the corresponding cylinder. The calculated powers of the two first-stage cylinders were 698 kW and 694 kW, while those of the two second-stage cylinders were 883 kW and 882 kW. The close values between cylinders in the same stage indicate that the phase arrangement and flow distribution of the paired cylinders are reasonably balanced. The higher power of the second-stage cylinders is mainly attributed to the much higher pressure level and the lower compressibility of ethylene under ultra-high pressure, which cause a steeper pressure rise for a given volume reduction.

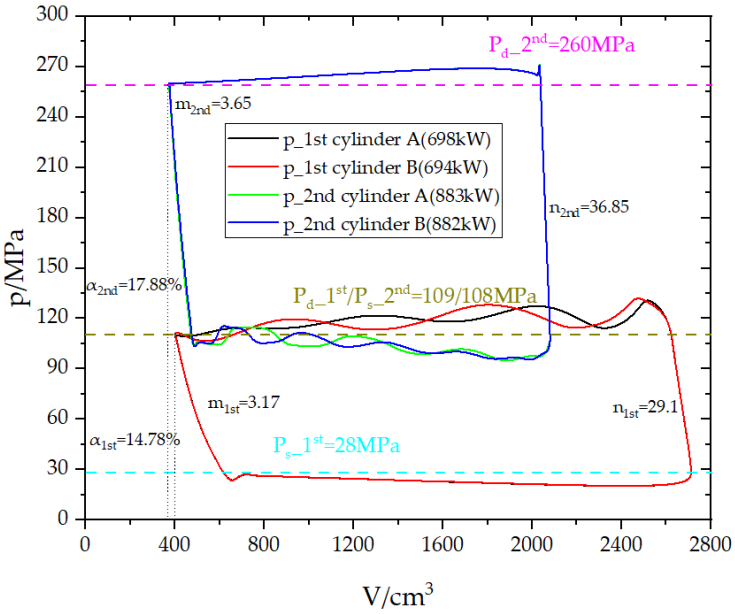


Figure 14. p–V diagrams inside the four cylinders.

It should be noted that the polytropic indices obtained from the p–V curves are effective indices fitted from the start and end states of the compression and expansion processes, rather than ideal-gas constants. For common gas compressors, the polytropic index is usually close to the isentropic index. However, ethylene under the present ultra-high-pressure condition exhibits strong real-gas behavior. Its density is high, its compressibility is greatly reduced, and its sound speed is significantly increased. As a result, a small reduction in chamber volume can lead to a sharp pressure increase, which produces a very steep compression curve and consequently a much larger effective polytropic index. The second-stage compression index is higher than that of the first stage because the second-stage process occurs at a higher pressure level, where ethylene behaves more like a dense fluid with lower compressibility.

4.2. Simulated Pressure Pulsation Inside the Interstage Pipeline

As shown in Figure 15, the pressure of 14 points was monitored while solving the numerical model. The monitored pressures fluctuated significantly over one cycle with multiple peaks and valleys. The pressure pulsation amplitude was employed to evaluate these fluctuations quantitatively and was defined as the ratio of the difference between the maximal pressure and the minimum pressure compared to the average pressure in one

cycle. Then, the pressure pulsation amplitudes of the 14 monitored points were calculated as 16.20%, 10.11%, 17.50%, 10.55%, 10.16%, 8.59%, 9.81%, 8.59%, 8.14%, 11.81%, 12.01%, 15.56%, 12.00% and 16.22%, as shown in Figure 15. The pressure amplitudes located close to the discharge ports of the first-stage cylinders (TP1 and TP3) were slightly larger than those close to the discharge buffer tank (TP2 and TP4), and significantly larger than those flowing through the buffer tank (TP6, TP7, TP8, and TP9). This was the same for pressure pulsations close to the suction pipeline of the second-stage cylinders.

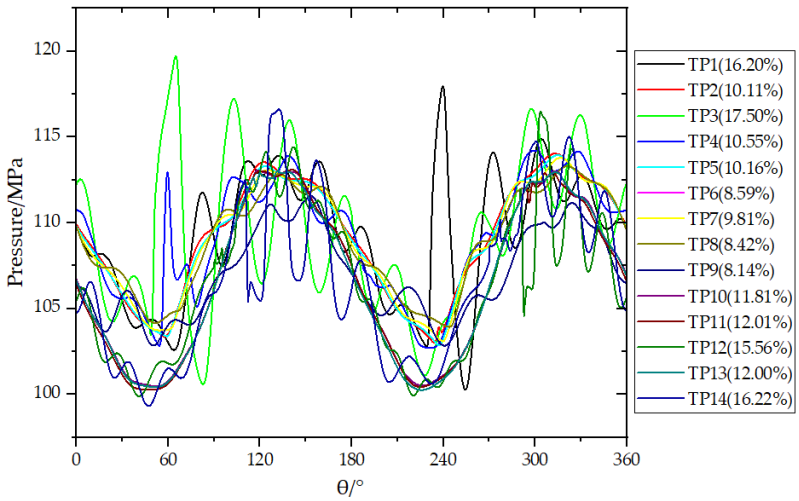


Figure 15. Pressure pulsation of the 14 monitored points inside the interstage pipeline.

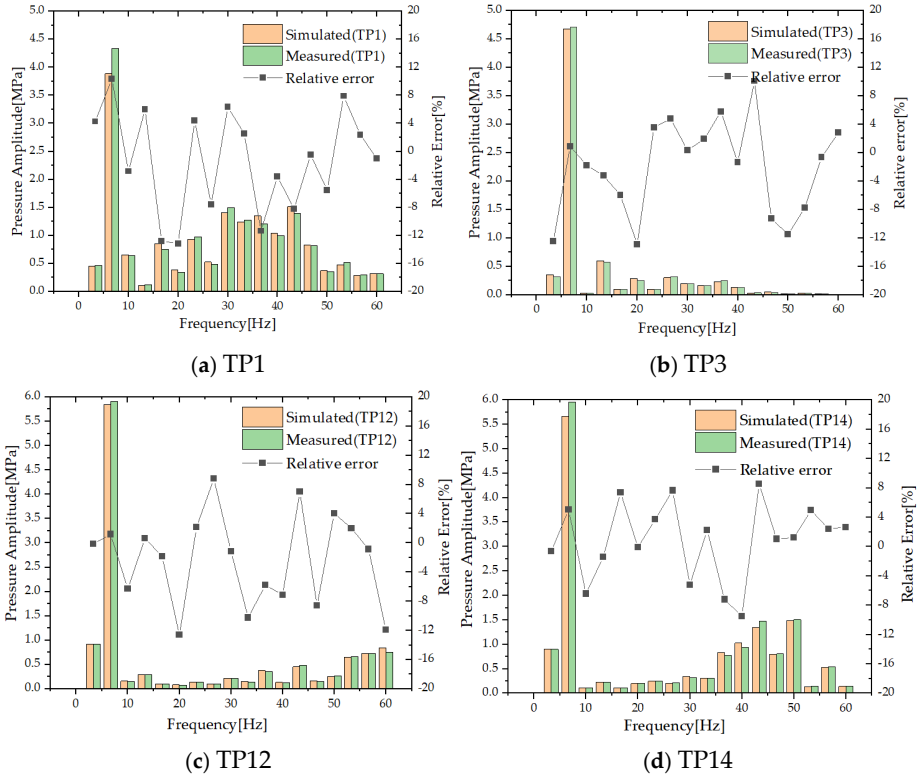
The spatial distribution of pressure pulsation shows a clear relationship with the excitation sources and pipeline components. TP1 and TP3, which are located close to the first-stage discharge ports, showed the largest pulsation amplitudes of 16.20% and 17.50%, respectively. These high values are caused by the intermittent discharge flow from the first-stage cylinders. After the flow passed through the discharge buffer tank and the interstage cooler network, the pulsation amplitude decreased. For example, the amplitude decreased from 16.20% at TP1 to 10.11% at TP2, and from 17.50% at TP3 to 10.55% at TP4, corresponding to reductions of approximately 37.6% and 39.7%, respectively. The lowest amplitude, 8.14%, occurred at TP9, which is approximately 53.5% lower than the maximum value at TP3. This indicates that the buffer tank, branch pipelines, cooler tubes, and pipe friction can attenuate pressure pulsation, but the attenuation is not sufficient to eliminate the pulsation completely.

Near the second-stage suction side, the pulsation amplitude increased again. TP12 and TP14 showed amplitudes of 15.56% and 16.22%, respectively. This increase is associated with the periodic suction demand of the second-stage cylinders and the opening and closing of the suction poppet valves. The multiple peaks and valleys in the pressure waveform are caused by the superposition of the first-stage discharge excitation, second-stage suction excitation, and wave reflection at the buffer tanks, branch connections, cooler manifolds, and elbows.

From an engineering perspective, TP1, TP3, TP12, and TP14 should be regarded as high-risk locations for subsequent vibration and fatigue assessment. The pressure pulsation field obtained from the CFD model can provide dynamic pressure loads for evaluating elbows, branch connections, buffer tank nozzles, cooler headers, and compressor cylinder flanges. These results can also guide the optimization of support stiffness, support locations, buffer volume, and acoustic attenuation measures.

4.3. Comparison Between the Simulated and Measured Pressure Pulsation

Despite the pressure pulsation amplitudes being employed to quantitatively evaluate pressure pulsation, it was insufficient to describe its characteristics. The pressure pulsation could lead to mechanical vibration in the pipeline and, in the most serious condition, induce pipeline resonance and excessive cyclic stress. Hence, the characteristics in the frequency domain should be analyzed. By using the Discrete Fourier Transform (DFT), the pressure pulsation in the time domain shown in Figure 15 was transferred into a distribution of frequency vs. amplitudes. Both the simulated and measured pressure pulsations at the discharge port of the first-stage cylinders and at the suction port of the second-stage cylinders, i.e., TP1, TP3, TP12, and TP14, are shown in Figures 16a, 16b and 16c, and 16d, respectively. It can be seen from these figures that the maximal amplitudes of the four test points were 6.67 Hz, which is twice the fundamental frequency of 3.33 Hz at a rotational speed of 200 rpm. This was because there were two working cylinders at the first stage of the hyper-compressor with two suction and discharge processes per cycle. The maximal discrepancies were −12.77%, −11.49%, −12.61%, and −12.11% at the 5th harmonic frequency of TP1, 15th harmonic frequency of TP3, 6th harmonic frequency of TP12, and 15th harmonic frequency of TP14, as shown in Figure 16.



(**a**) TP1 (**b**) TP3

(**c**) TP12 (**d**) TP14

Figure 16. Frequency vs. amplitude of pressure pulsation at four cylinders.

The quantitative comparison between the CFD prediction and strain gauge measurement was further evaluated using RMSE (Root Mean Square Error) and MAPE (Mean Absolute Percentage Error), defined as

$$\mathrm{RMSE} = \sqrt{\frac{1}{n}\sum_{i=1}^{n}\left(Simulated_i - Measured_i\right)^2} \tag{15}$$

$$\mathrm{MAPE} = \frac{1}{n}\sum_{i=1}^{n}\frac{\left(Simulated_i - Measured_i\right)}{Measured_i} \times 100\% \tag{16}$$

The RMSE, MAPE and MRE (Maximal Relative Error) of the 14 test points are listed in Table 5. The MAPE values of the fourteen test points ranged from 4.661% to 6.441%, with an average value of 5.651%. The RMSE values ranged from 0.015 MPa to 0.104 MPa, depending on the local pressure pulsation amplitude. The maximum relative error among all test points was 12.77%, which indicates that the discrepancies of the dominant harmonic amplitudes were generally within approximately 13%. These results demonstrate that the proposed CFD model can predict the pressure pulsation characteristics of the interstage pipeline with acceptable accuracy. The relatively larger maximum errors at several points may be attributed to local valve impact dynamics, structural vibration coupling in strain gauge measurements, and numerical dissipation of higher harmonic components.

Table 5. RMSE, MAPE and MRE of the 14 test points.

Test Point	RMSE [MPa]	MAPE [%]	MRE [%]
TP1	0.082	5.348	12.77
TP2	0.038	6.316	11.37
TP3	0.015	6.245	11.49
TP4	0.103	5.565	11.351
TP5	0.082	5.704	11.676
TP6	0.027	5.962	11.546
TP7	0.018	4.918	9.67
TP8	0.017	5.74	10.488
TP9	0.071	5.577	10.901
TP10	0.090	4.661	9.949
TP11	0.050	5.088	11.985
TP12	0.029	6.17	12.61
TP13	0.104	5.378	10.804
TP14	0.081	6.441	12.11

The discrepancies at higher harmonics were larger than those at lower harmonics. Several factors may contribute to this phenomenon. First, the equivalent single-channel valve model preserves the global flow area and flow resistance of the multi-poppet valve, but it may smooth local jet interaction, circumferential flow non-uniformity, and poppet-to-poppet differences. As a result, localized losses and high-frequency pressure components may be underestimated. Second, valve impact, rapid closing, and possible rebound of the poppet can generate short-duration pressure waves. These transient events are difficult to fully resolve using the present dynamic mesh and time step. Third, the strain gauge measures the total surface strain of the pipe. Although the test points were arranged away from nozzles, flanges, and supports, a small portion of the measured strain may still originate from pipe wall vibration or bending deformation rather than internal pressure alone. This structural vibration coupling is more likely to affect higher-frequency components. Finally, numerical dissipation introduced by the RANS turbulence model, spatial discretization, and second-order temporal scheme may also attenuate high-frequency pressure amplitudes. Therefore, the lower-harmonic components are expected to be predicted more accurately than the higher-harmonic components.

The predicted pressure pulsation levels have direct engineering implications for LDPE hyper-compressor design and operation. In the present case, the maximum pressure pulsations near the first-stage discharge and second-stage suction sides were approximately

16–18%. Such pressure fluctuations may generate alternating forces at elbows, tees, buffer tank nozzles, cooler connections, and compressor cylinder flanges. Therefore, the pressure pulsation field obtained from the CFD model can be used as an input for mechanical vibration, cyclic stress, and fatigue life assessments of the interstage pipeline.

For support design, the locations with high pressure pulsation amplitudes should be examined together with the structural natural frequencies of the pipeline system. Support stiffness, support spacing, and local constraints should be optimized to avoid the coincidence between acoustic excitation frequencies and structural natural frequencies. In particular, supports near branch connections, buffer tanks, and cooler manifolds should be designed to reduce vibration amplification while avoiding excessive local constraint stress.

For acoustic dampening, the predicted frequency domain pressure amplitudes can be used to evaluate whether the existing buffer tanks, coolers, and pipeline lengths are sufficient to attenuate the dominant harmonics. If excessive pulsation remains, possible mitigation strategies include modifying the pipeline layout, adjusting branch lengths to avoid acoustic resonance, increasing local damping, optimizing buffer volume, or adding pulsation attenuation devices. The present CFD framework can therefore support both design-stage pulsation control and operation-stage diagnosis of LDPE hyper-compressors.

5. Conclusions

In this study, a coupled transient CFD framework was developed to investigate the pressure pulsation in the interstage pipeline of an LDPE hyper-compressor. Different from conventional plane–wave methods and 1D unsteady-flow models, the proposed framework integrates real-gas thermodynamic properties of ethylene, dynamic poppet valve motion, compression chamber processes, full three-dimensional interstage pipeline geometry, and non-intrusive strain gauge validation. The main conclusions are as follows:

(1) The equivalent single-channel representation of the multi-poppet valve, combined with a single-degree-of-freedom valve dynamics equation, enabled the transient interaction between poppet motion, chamber pressure, and pipeline pulsation to be considered in the full CFD model. This coupling is difficult to represent using conventional plane–wave models, which are based on small-perturbation assumptions, or 1D models, which simplify the complex three-dimensional flow passages and branch structures.

(2) The proposed CFD model captured the coupled thermodynamic process in the working chambers and the pressure pulsation propagation in the interstage pipeline. The calculated p–θ and p–V diagrams showed that the polytropic indices of the compression and expansion processes were much higher than those of common gas compressors. This behavior is mainly associated with the low compressibility and real-gas characteristics of ethylene under ultra-high pressure.

(3) Significant pressure pulsations were predicted in the interstage pipeline. The pressure pulsations near the first-stage discharge ports reached 16.2% and 17.5%, while those near the second-stage suction ports reached 15.56% and 16.22%. These results indicate that pulsation-induced cyclic stress should be considered in the design of cylinders, branch pipelines, buffer tank nozzles, cooler connections, and pipe supports. The predicted pressure field can provide dynamic loads for subsequent vibration, fatigue life, and acoustic-attenuation analyses.

(4) The predicted frequency domain characteristics agreed reasonably with the strain gauge measurements. The discrepancies of the dominant harmonic amplitudes were generally within approximately $\pm$13%, and the lower harmonic components were predicted more accurately than the higher harmonics. This indicates that the proposed CFD–valve-dynamics–field-validation framework can be used not only for pressure pulsation pre-

diction but also for field diagnosis of LDPE hyper-compressors by comparing measured spectra with simulated harmonic characteristics.

(5) The present method advances the design and diagnostic capability of LDPE hyper-compressors by linking internal valve/chamber dynamics with pipeline-scale pressure pulsation and non-intrusive field measurement. It can help identify high-risk pulsation locations, evaluate the effectiveness of existing buffer tanks and supports, and guide future optimization of pipeline layout, support stiffness, and pulsation attenuation strategies. Future work will further improve the representation of multi-poppet valve non-uniformity and investigate transient operating conditions such as start-up, shutdown, and valve malfunction.

Author Contributions: Conceptualization, X.C. and B.Z.; Investigation, W.X.; Methodology, L.M., X.C. and B.Z.; Writing—original draft, L.M. and B.Z.; Writing—review and editing, Z.M. All authors have read and agreed to the published version of the manuscript.

Funding: This work was supported by the National Natural Science Foundation of China [Grant No. 52106054] and the China Postdoctoral Science Foundation [Grant No. 2018M643639].

Data Availability Statement: The data presented in this study are available on request from the corresponding author. (The data are not publicly available due to privacy or ethical restrictions).

Conflicts of Interest: Liya Ma and Zenghui Ma were employed by the company Xinjiang Oilfield Gas Storage Co., Ltd. The remaining authors declare that the research was conducted in the absence of any commercial or financial relationships that could be construed as a potential conflict of interest.

References

1. Santagata, C.; Iaquaniello, G.; Salladini, A.; Agostini, E.; Capocelli, M.; De Falco, M. Production of low-density poly-ethylene (LDPE) from chemical recycling of plastic waste: Process analysis. *J. Clean. Prod.* **2020**, *253*, 119837. [CrossRef]
2. Giacomelli, E.; Battagli, P.; Campo, N.; Graziani, F. Autofrettaging procedures on LDPE hyper-compressor components. In Proceedings of the ASME Pressure Vessels and Piping Conference, Vancouver, BC, Canada, 23–27 July 2006; Volume 4756, pp. 47–56.
3. Giacomelli, E.; Battagli, P.; Lumachi, F.; Gimignani, L. Safety Aspects of design of cylinders and hyper-compressors for LDPE. In Proceedings of the ASME Pressure Vessels and Piping Conference, San Diego, CA, USA, 25–29 July 2004; Volume 46687, pp. 63–71.
4. Agostini, M.; Carcasci, C.; Cristofani, A. Managing Transient Operating Conditions of Hyper Compressors. In *Proceedings of the Pressure Vessels and Piping Conference*; American Society of Mechanical Engineers: New York, NY, USA, 2014; Volume 46025, p. V005T05A002.
5. MacLaren, J.F.T.; Tramschek, A.B.; Sanjines, A.; Pastrana, O.F. A comparison of numerical solutions of the unsteady flow equations applied to reciprocating compressor systems. *J. Mech. Eng. Sci.* **1975**, *17*, 271–279. [CrossRef]
6. Giacomelli, E.; Falciani, F.; Volterrani, G.; Fani, R.; Galli, L. Simulation of cylinder valves for reciprocating compressors. In Proceedings of the Engineering Systems Design and Analysis, Torino, Italy, 4–7 July 2006; Volume 42487, pp. 949–958.
7. Bianchini, M.; Campo, N.; Francini, S.; Vidyasagar, R. Advances in dynamic analysis for hypercompressor cylinder valves. In Proceedings of the ASME Pressure Vessels and Piping Conference, Chicago, IL, USA, 27–31 July 2008; Volume 48289, pp. 111–121.
8. Bagagli, R.; Campo, N.; Francini, S.; Simpson, K.C.; Morgan, C. Methods for Life Assessment of Hypercompressor Poppet Valves. In Proceedings of the Pressure Vessels and Piping Conference, Bellevue, WA, USA, 18–22 July 2010; Volume 49248, pp. 85–92.
9. Maggi, C.; Wojnar, J.; Bagagli, R.; Tognarelli, L. Improved Accuracy on Efficiency of PK Hypercompressor Valves. In *Proceedings of the Pressure Vessels and Piping Conference*; American Society of Mechanical Engineers: New York, NY, USA, 2014; Volume 46025, p. V005T05A004.
10. Simpson, K.; Sanford, J.; Finnefrock, L. Redesign of LDPE Secondary Compressor Valves to Better Tolerate Polyethylene Wax Fouling. In *Proceedings of the Pressure Vessels and Piping Conference*; American Society of Mechanical Engineers: New York, NY, USA, 2016; Volume 50411, p. V005T05A004.
11. Maggi, C.; Tognarelli, L.; Capanni, A.; Wojnar, J. New manufacturing cycle to improve the life of packing cups for hyper-compressors. In *Proceedings of the Pressure Vessels and Piping Conference*; American Society of Mechanical Engineers: New York, NY, USA, 2012; Volume 55041, pp. 27–36.
12. Stosiak, M.; Karpenko, M.; Ivannikova, V.; Maskeliūnaitė, L. The impact of mechanical vibrations on pressure pulsation, considering the nonlinearity of the hydraulic valve. *J. Low Freq. Noise Vib. Act. Control.* **2025**, *44*, 706–719. [CrossRef]

13. Lei, D.; Li, X.; Li, Y.; Ren, X. Design of packing cup interference fit value of hypercompressors for low density polyethylene production. *Front. Energy* **2019**, *13*, 107–113.
14. Miller, E.S.; Blanding, J.M. Strain gage and thermocouple measurements of hyper compressor packing cups to study pressure sealing performance. In *Proceedings of the Pressure Vessels and Piping Conference*; American Society of Mechanical Engineers: New York, NY, USA, 2015; Volume 56987, p. V005T05A003.
15. Park, B.E.; Kim, J.S.; Lee, J.K.; Lee, I.B. Anomaly detection in a hyper-compressor in low-density polyethylene manufacturing processes using WPCA-based principal component control limit. *Korean J. Chem. Eng.* **2020**, *37*, 11–18. [CrossRef]
16. Giacomelli, E.; Passeri, M.; Giusti, S.; Zagli, F.; Generosi, S. Modeling of Pressure Pulsations for LDPE Reciprocating Compressors and Interaction with Mechanical System. In Proceedings of the Engineering Systems Design and Analysis, Manchesterc, UK, 19–22 July 2004; Volume 41731, pp. 945–952.
17. Karpenko, M. Aircraft hydraulic drive energy losses and operation delay associated with the pipeline and fitting connections. *Aviation* **2024**, *28*, 1–8. [CrossRef]
18. Bai, W.J.; Li, Y.Q.; Duan, Q. Vibration Analysis and Transformation of Hyper Compressor Pipeline for LDPE Plants. In *Proceedings of the ASME International Mechanical Engineering Congress and Exposition*; American Society of Mechanical Engineers: New York, NY, USA, 2013; Volume 56437, p. V014T15A015.
19. Carcasci, C.; Sacco, M. Preventing Failures In LDPE Plants Caused By Vibrations And Pulsations Of Reciprocating Compressors. In *Proceedings of the Abu Dhabi International Petroleum Exhibition and Conference*; SPE: Richardson, TX, USA, 2017; p. D031S076R003.
20. Carcasci, C.; Sacco, M.; Landucci, M.; Fiaschi, M. From piping deformation to pressure pulsation measurements to solve LDPE plants vibration issues. In *Proceedings of the Pressure Vessels and Piping Conference*; American Society of Mechanical Engineers: New York, NY, USA, 2018; Volume 51661, p. V005T05A003.
21. Fusi, A.; Cappelli, L.; Carcasci, C.; Sacco, M. Tuning of the acoustical analysis model for hypercompressors through strain gage pulsation measurements. In *Proceedings of the Pressure Vessels and Piping Conference*; American Society of Mechanical Engineers: New York, NY, USA, 2019; Volume 58967, p. V005T05A008.
22. Geng, M.; Xiao, J.; Qian, Z.; Liu, S.; Zhang, C.; Wang, L.; Yu, X.; Wang, X. Analysis of Pressure Pulsation in Hypercompressor Pipeline. In *Proceedings of the Pressure Vessels and Piping Conference*; American Society of Mechanical Engineers: New York, NY, USA, 2022; Volume 86168, p. V003T05A001.
23. Xiao, J.; Geng, M. Analysis and treatment of gas pulsation in the pipeline of a hyper compressor. *Proc. Inst. Mech. Eng. Part E J. Process Mech. Eng.* **2023**, *238*, 2404–2415. [CrossRef]
24. Yang, L.; Jia, X.; Peng, X. Analysis of the Thermodynamic Characteristics of a Hyper-Compressor through Numerical Simulation and Experimental Investigation. *Appl. Sci.* **2023**, *13*, 4478. [CrossRef]
25. Stosiak, M.; Bury, P.; Karpenko, M. The influence of hydraulic hose length on dynamic pressure waveforms including wave phenomena. *Sci. Rep.* **2025**, *15*, 31548. [CrossRef] [PubMed]
26. Zhao, B.; Wei, H.; Zhai, Y.; Feng, J.; Peng, X. Application of CFD Method to Investigate the Evolution of the Thermodynamic Parameters of a Hyper Compressor and Its Pipelines. *Energies* **2022**, *15*, 4452. [CrossRef]
27. Smukala, J.; Span, R.; Wagner, W. New equation of state for ethylene covering the fluid region for temperatures from the melting line to 450 K at pressures up to 300 MPa. *J. Phys. Chem. Ref. Data* **2000**, *29*, 1053–1121. [CrossRef]
28. Zhao, B.; Jia, X.; Sun, S.; Wen, J.; Peng, X. FSI model of valve motion and pressure pulsation for investigating thermodynamic process and internal flow inside a reciprocating compressor. *Appl. Therm. Eng.* **2018**, *131*, 998–1007. [CrossRef]

Disclaimer/Publisher's Note: The statements, opinions and data contained in all publications are solely those of the individual author(s) and contributor(s) and not of MDPI and/or the editor(s). MDPI and/or the editor(s) disclaim responsibility for any injury to people or property resulting from any ideas, methods, instructions or products referred to in the content.